

PROPER MOTIONS OF YOUNG STELLAR OUTFLOWS IN THE MID-INFRARED WITH SPITZER (IRAC). I. THE NGC 1333 REGION

A. C. RAGA¹

¹ Instituto de Ciencias Nucleares, UNAM, Ap. 70-543, 04510 D.F., Mexico

A. NORIEGA-CRESPO²

² Infrared Processing and Analysis Center, California Institute of Technology, Pasadena, CA 91125, USA

S. J. CAREY³

³ Spitzer Science Center, California Institute of Technology, Pasadena, CA 91125, USA

H. G. ARCE⁴

⁴ Department of Astronomy, Yale University, New Haven, CT 06520, USA

Draft version October 29, 2018

ABSTRACT

We use two 4.5 μ m Spitzer (IRAC) maps of the NGC 1333 region taken over a ~ 7 yr interval to determine proper motions of its associated outflows. This is a first, successful attempt at obtaining proper motions of stellar outflow from Spitzer observations. For the outflow formed by the Herbig-Haro objects HH7, 8 and 10, we find proper motions of ~ 9 -13 km s⁻¹, which are consistent with previously determined optical proper motions of these objects. We determine proper motions for a total of 8 outflows, ranging from ~ 10 to 100 km s⁻¹. The derived proper motions show that out of these 8 outflows, 3 have tangential velocities ≤ 20 km s⁻¹. This result shows that a large fraction of the observed outflows have low intrinsic velocities, and that the low proper motions are not merely a projection effect.

Subject headings: ISM: jets and outflows — ISM: Herbig-Haro objects — ISM: star formation — circumstellar matter — stars: formation — infrared: ISM — ISM: individual objects (HH7-11) — ISM: individual objects (NGC 1333)

1. INTRODUCTION

Starting with the work of Herbig & Jones (1981), who studied the HH 1/2 outflow, the study of proper motions of Herbig-Haro (HH) objects has become one of the fundamental tools in exploring the properties of outflows from young stars. Proper motions of young stellar outflows were first measured at radio wavelengths by Rodríguez et al. (1989), who studied the Serpens “triple source”. Later, Noriega-Crespo et al. (1997) first obtained proper motions of outflows at IR wavelengths of HH1, from H₂ 2.12 μ m images.

In contrast to what has happened at optical and radio wavelengths, the study of IR proper motions of young stellar outflows has not flourished. This is probably due to the fact that older IR images typically cover only relatively small fields, so that it is many times impossible to obtain a good centering/scaling between them and newer (larger field) IR images. Previous IR proper motion studies include Noriega-Crespo et al. (1997: HH1), Chrysostomou et al. (2000: HH7-11, 25-26 and 33/40) and Raines et al. (2000: GGD37).

In this paper we make a first attempt to measure proper motions from Spitzer-IRAC IR images of young stellar outflows. This is possible because even though

the IRAC pixels are relatively large (1".2), some outflows have now been observed over time intervals of ~ 10 yr. For example, for an outflow with plane-of-the-sky velocities of ~ 100 km s⁻¹ at a distance of ~ 500 pc, offsets of ~ 0.35 pixels are expected over ~ 10 yr. As shown initially by Raga, Barnes & Mateo (1990), such offsets can be measured with reasonable accuracy in CCD images of stellar outflows.

There are three fundamental reasons that allow us to use IRAC to measure proper motions in the mid-IR, despite its relative low angular resolution (FWHM $\sim 2''$) in comparison with optical or near-IR ground based observations. First of all is the outstanding stability of the pointing control system of the Spitzer Space Telescope over the past nine years. Secondly, the unchanged performance of its optical system and its detectors. Thirdly, the ability of IRAC to map large regions of the sky, thus providing plenty of point sources that can be used to create and fix a reliable reference frame to compare observations from different epochs.

We study two 4.5 μ m IRAC frames of the NGC 1333 region, obtained in February/September 2004 and October/November 2011. These observations are described in detail in section 2.

These images allow us to obtain the proper motions of some of the HH7-11 knots (HH7, 8 and 10), which can be compared with previous optical (Herbig & Jones 1983; Noriega-Crespo & Garnavich 2001) and IR (Chrysosto-

raga@nucleares.unam.mx
alberto@ipac.caltech.edu
carey@ipac.caltech.edu
hector.arce@yale.edu

et al. 2000) proper motion measurements of this outflow. This is done in section 3. Also, these images allow us to obtain the proper motions of other outflows in NGC 1333, as described in section 4. Finally, our results are summarized in section 5.

2. OBSERVATIONS

NGC 1333 was one of the first star forming regions observed with the Spitzer Space Telescope (Werner et al. 2004) with the Infrared Array Camera (IRAC) (Fazio et al. 2004) during the Cryo-mission as part of the IRAC GTO program of its principal investigator (PI) (PID 6, G. Fazio). This first epoch was complemented approximately six months later by the Cores-to-Disks Spitzer Legacy program as part of their mapping of the Perseus molecular cloud (PID 178, PI N. Evans).

Multiple epoch observations of star forming regions relatively near the ecliptical plane are essential to weed out asteroids when trying to identify real proto-stellar objects (see e.g. Evans et al. 2009). The more recent data were obtained in October–November 2011, and are being currently analyzed to study the time variability of young stellar objects (YSOs) in the region, as part of the Warm-mission Spitzer Exploration program YSOVAR (PID 61026, PI J. Stauffer). YSOVAR has observed the core of NGC 1333, a $\sim 16' \times 11'$ region centered on 03h29m10.175s +31d16m16.0s, over a period of nearly a month using 73 different visits. Each visit lasted approximately 15 minutes with a mean coverage of $\sim 4 - 5$ in the final maps, although some pixels in the overlap regions can double these values. Our final 2010 image has a mean coverage of ~ 300 , i.e., on average each pixel has seen the object some 300 times, and since the observing time per pixel is 12 sec, this corresponds to a \sim one hour total exposure time.

This central map has determined the size of the region that we have used for our analysis of the proper motions between the two (2004 & 2011) available epochs. The final map is actually a bit smaller to avoid the scattered light present around the very bright young star LZK 12 in the very deep YSOVAR image. The Cryo-mission observations were carried using all IRAC channels (3.6, 4.5, 5.8 & $8.0\mu\text{m}$), while in the Warm-mission observations we can only use channels 1 and 2 (3.6 and $4.5\mu\text{m}$). For the three mentioned programs, the data was collected using the High-Dynamic-Range (HDR) mode with a 12sec integration time for the 'long' frames and 0.6sec for the 'short' ones. For the purpose of our analysis we have concentrated on the data at $4.5\mu\text{m}$, which for young stellar outflows has proven to be a very good tracer of the molecular Hydrogen emission of some of the bright pure rotational transitions [(0-0 S(9) at 4.6947 , 0-0 S(10) at 4.4096 and 0-0 S(11) at $4.1810\mu\text{m}$], and therefore, of their shock excited emission (Noriega-Crespo et al. 2004a,b; Looney et al. 2007; Tobin et al. 2007; Ybarra & Lada 2009; Maret et al. 2009; Raga et al. 2011; Noriega-Crespo & Raga 2012).

For the IRAC observations we have used the latest versions of the data, S18.18.0 (Cryo) and S19.0.0 (Warm), and a scale of $0.3''/\text{pix}$ for the final maps, i. e. a seventh of the IRAC FWHM $\sim 2''$ angular resolution. The maps of the different epochs are created with the same fiducial frame, using MOPEX (Makovoz, Khan & Masci 2006), which brings them very close to the same frame of refer-

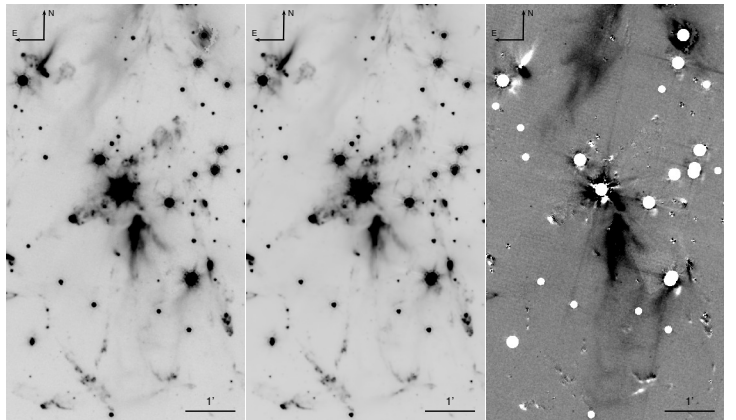


Figure 1. Top frame: 2004–2011 difference image. Center: 2011 image. Bottom: 2004 image. In the difference image, the knots along outflows with proper motions show up as “positive/negative” double ridge structures, and the white disks are masked stars.

ence. A dozen non-saturated stars common between the two epochs are then used for the final alignment of the images, with a typical centroid accuracy of less than a tenth of a pixel. The two resulting maps (2004 and 2011) are shown in Figure 1.

Figure 1 shows the two final images (2004 and 2011), and the difference between these two images. In the difference map, one can clearly see that some of the compact emission features show clear proper motions. For example, a bow-shaped region in the SW region of the frame shows a “positive/negative” ridge combination which clearly indicates a motion of this feature. Such motions are analyzed in detail below.

Although there are no major changes in the optics of the telescope or the performance of the detectors between the IRAC Cryo and Warm missions, a comparison between the 2004 and 2011 images shows stronger optical ghosts around the bright sources in the Warm data. This effect is probably enhanced because of the very deep coverage of the YSOVAR data (with ~ 300 exposures of 12 sec for each pixel, see above). Figure 2 shows a $3.5' \times 3.5'$ region of NGC 1333 with some bright sources, where one can see the typical ‘heart shape’ IRAC Point Spread Function, with the nearby “triangular ghosts” marked with the white boxes ($12'' \times 12''$). These are an annoyance more than a problem in measuring the proper motions, since they appear as real time variations between epochs. For this reason we have masked some of them in both final (2004 and 2011) images. The observations are summarized in Table 1.

3. THE HH7-11 OUTFLOW

In Figure 3, we show the 2004 frame of the HH7-11 outflow. HH 9 is not seen in the $4.5\mu\text{m}$ IRAC maps, and HH11 is lost within the PSF of SVS13. The image shows a knot $\approx 20''$ to the S of HH10, which we have labeled “knot A” (see Figure 3).

Figure 3 also shows proper motion vectors calculated with the “proper motion mapping” technique described by Raga et al. (2012). This (rather simplistic) technique is described in Appendix A. In particular, the HH7-11 proper motions shown in Figure 3 were computed with cross correlations in boxes of size $L = 30$ pixels (with each pixel corresponding to $0''.3$, see section 2) which have peak fluxes of at least $f_{min} = 2.0$ mJy/sterad (see

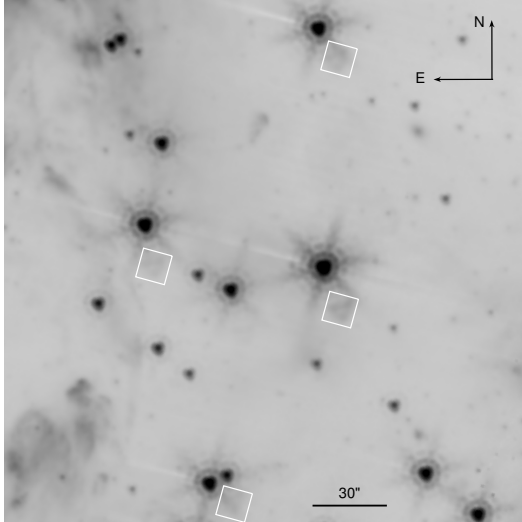


Figure 2. Region of the “Warm” (2011) analyzed frame. The white boxes indicate the “ghost” structure associated with the PSF in this frame (see section 2).

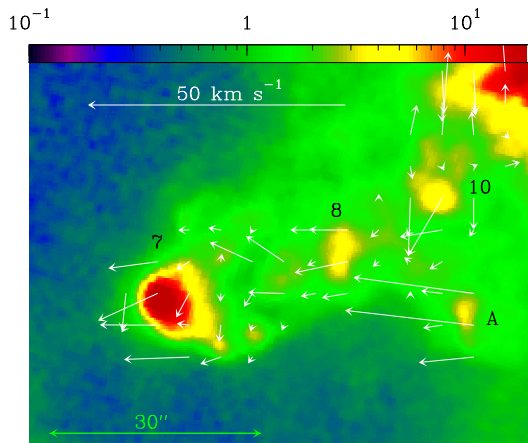


Figure 3. The map shows HH7-11 outflow lobe in the 2004 map. The white arrows indicate the proper motion velocities (for a distance of 220 pc to the system) computed within the cross correlation boxes with high enough intensities. We detect motions for HH 7, 8 and 10 (HH 11 being confused with the stellar PFS off the NW corner of the frame). N is up and E to the left. The image is displayed with a logarithmic scale given (in mJy/sterad) by the top bar.

Appendix A). The proper motion velocities were calculated assuming a distance of 220 pc to NGC 1333 (Černis 1990; Hirota et al. 2008).

The HH7, 8 and 10 knots have velocities $\approx (10 \pm 4)$ km s $^{-1}$ (HH7: 13 km s $^{-1}$; HH8: 10 km s $^{-1}$; HH10: 9 km s $^{-1}$), with HH7 and HH8 moving approximately parallel to the outflow axis, and HH10 showing a possibly significant deviation towards the S. These proper motions were obtained by averaging the proper motions from the two boxes closest to the peak emission of the knots. Also the region between HH7 and 8 shows filamentary structures which apparently share the kinematics of these two HH knots (see Figure 3).

Knot A has a significantly higher proper motion velocity of (25 ± 4) km s $^{-1}$, pointing approximately E. This knot could belong to one of the other outflows present in this complex region (see section 4 and Davis et al. 2011).

Finally, relatively large proper motions are seen within

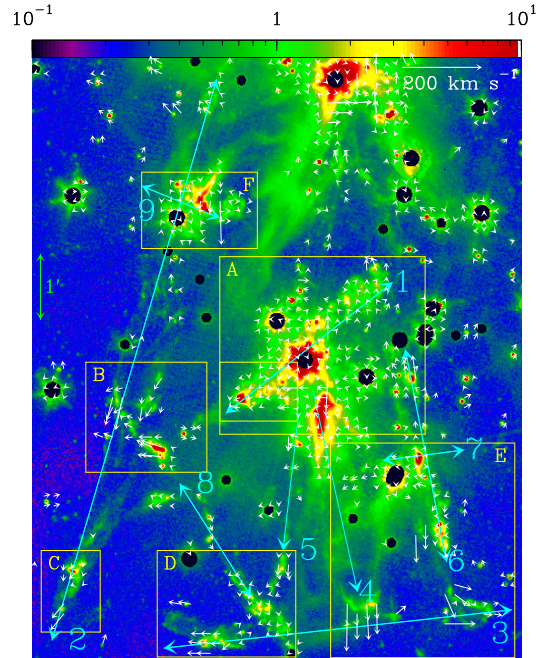


Figure 4. 2004 frame (displayed with the logarithmic scale given in mJy/sterad by the top bar) of the studied field. The dark, circular regions correspond to masked stars. The blue arrows indicate the axes of the outflows described by Davis et al. (2008), which we have numbered 1 through 9. The yellow boxes (labeled A through F) indicate interesting subfields, which are shown in an expanded scale in Figures 5-10. The white arrows indicate the proper motion velocities (for a distance of 220 pc) obtained through our “cross correlation mapping” technique. N is up and E to the left.

$\sim 20''$ from the SVS13 outflow source (outside the upper, right hand side corner of Figure 3), which are probably related with the spikes of the PSF, and are unlikely to represent real motions in the flow.

The proper motions that we have obtained for HH 7, 8 and 10 are roughly consistent with the velocities of $\sim (20 \pm 10)$ km s $^{-1}$ determined for these knots with the proper motion determinations of Noriega-Crespo & Garnavich (2001), scaled to a distance of 220 pc to HH7-11. The proper motions of Herbig & Jones (1981) are also consistent with these relatively low velocities. The velocities of ~ 400 km s $^{-1}$ determined by Chrysostomou et al. (2000) are inconsistent with the three other independent (optical and IR) proper motion determinations.

4. OTHER OUTFLOWS

In Figure 4, we show a $450 \times 550''$ field (covered in the two epochs) approximately centered on the HH 7-11 outflow. On the 2004 frame, we show the axes of the molecular outflows (which we have numbered 1 through 9) described by Davis et al. (2008). As already seen in the difference image between the two epochs (see Figure 1 and section 2), there are several regions of extended emission which show detectable proper motions.

The proper motions shown in Figure 4 correspond to cross correlations within $L = 60$ ($18''$) pixel boxes of the two epochs, with fluxes of at least $f_{min} = 0.9$ mJy/sterad (see Appendix A).

We have chosen 6 regions (labeled A through F in Figure 4) which show the more interesting proper motion detections. These regions are described in the following subsections.

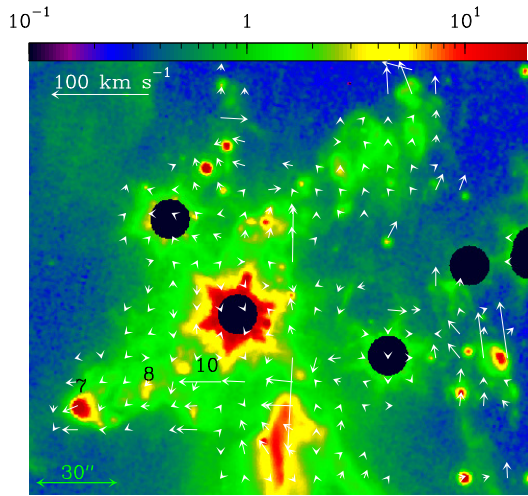


Figure 5. Subfield A of Figure 4. The 2004 map is shown together with the proper motion velocities. N is up and E to the left.

4.1. Region A

This region (see Figure 5) includes the HH 7-11 outflow (the smaller box within region A in Figure 4, corresponding to the blue-shifted, 7-11 lobe, is shown in Figure 3). It is clear that while organized proper motions (aligned with the outflow axis) are seen along the HH 7, 8, 10 knots, such motions are not seen in the NW outflow lobe.

To the S of the SVS 13 source, relatively large proper motions with Easterly direction are seen, but it is not clear that these motions are associated with well defined knots (except for “knot A” of Figure 3, see section 3). These motions might be associated with a previously undetected outflow.

In the center of the frame, at $\sim 30''$ from the Southern edge of the frame, we see a bow-like region with Northward proper motions of $\sim 10 \text{ km s}^{-1}$. These marginally detected motions could be associated with the Northern lobe of outflow 4 (see Figure 4).

Close to the SW corner of the frame, we see a region with a broken-up, bow-like structure with proper motion velocities of $\sim 20\text{-}70 \text{ km s}^{-1}$ to the N or NE. This motion appears to be shared by some of the knots seen in the NW region of Figure 5. All of these Northward directed knots appear to belong to outflow 6 (see Figure 4).

4.2. Region B

This region (see Figures 4 and 6) shows two systems of knots with different proper motions. One set of knots (in the Northern part of Figure 6) has proper motion velocities of $20\text{-}100 \text{ km s}^{-1}$ directed approximately to the SSE. This set of knots appears to be associated with outflow 2 (see Figure 4).

A second set of knots (in the Southern half of Figure 6) shows proper motions of similar magnitudes ($10\text{-}60 \text{ km s}^{-1}$), but directed Eastwards. These knots could be associated with outflow 8 (see Figure 4), though their motion would imply a substantial deflection from the outflow axis. Alternatively, these knots could belong to a previously undetected outflow.

4.3. Region C

This region (see Figures 4 and 7) shows knots with proper motions of $10\text{-}60 \text{ km s}^{-1}$ directed towards the

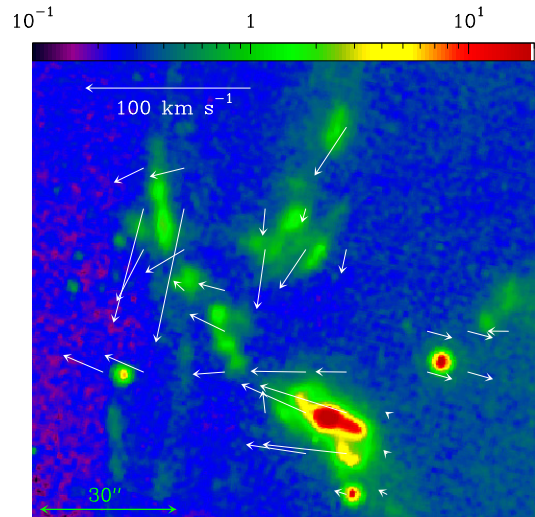


Figure 6. Subfield B of Figure 4. The 2004 map is shown together with the proper motion velocities. N is up and E to the left. SE. These knots are therefore likely to be a prolongation of the S lobe of outflow 2 (see Figure 4).

4.4. Region D

The Southern part of this region (Figure 8) shows a bow-like structure with Eastwards proper motions of $20\text{-}40 \text{ km s}^{-1}$, apparently associated with the E lobe of outflow 3 (see Figure 4). In the NW corner of the frame, we find a set of knots with Southward proper motions of $20\text{-}40 \text{ km s}^{-1}$, which are likely to be associated with outflow 5 (see Figure 4).

The region which is morphologically aligned with outflow 8 (extending from the N center to the SW corner of Figure 8) does not show proper motions aligned with the outflow axis.

4.5. Region E

In the SW corner of this region (Figure 9) we see a set of knots with Western proper motions of $10\text{-}80 \text{ km s}^{-1}$ which are morphologically and kinematically associated with the W lobe of outflow 3 (see Figure 4).

In the SE corner, we see a bow shaped structure with Southern proper motions of up to 100 km s^{-1} , which is likely to be associated with outflow 4. In the center of this region we see knots with Southern proper motions of $\sim 60 \text{ km s}^{-1}$ which might be associated with outflow 6 (see Figure 4).

Finally, in the NE corner of this field (see Figure 9) we see aligned proper motion vectors towards the E, corresponding to velocities $\sim 15 \text{ km s}^{-1}$. These motions could be associated with the Eastern lobe of outflow 7 (see Figure 4).

4.6. Region F

This region (Figure 10) shows some high Southwards proper motions of $\sim 50 \text{ km s}^{-1}$ (actually, one of the Southwards proper motion velocities is $> 100 \text{ km s}^{-1}$, but for a cross-correlation box without any clear feature), which do not have a clear identification with the outflows of Davis et al. (2008).

Also, this region might be showing evidence of a bipolar structure (with oppositely directed proper motion velocities of $\sim 10 \text{ km s}^{-1}$, indicated with two open circles

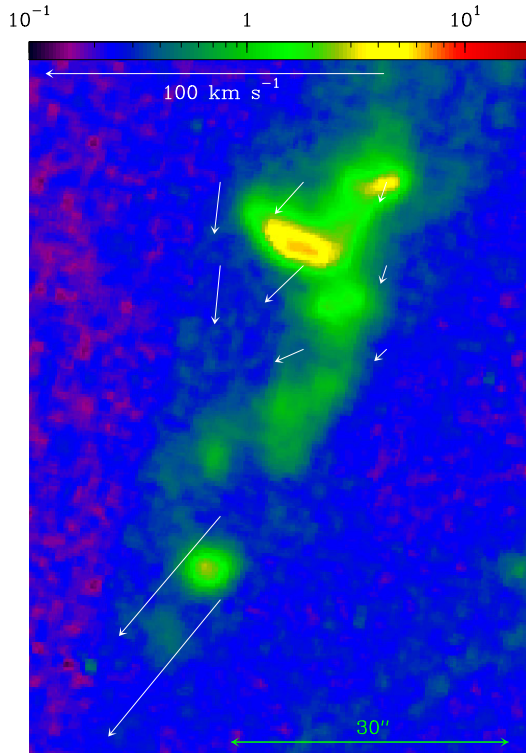


Figure 7. Subfield C of Figure 4. The 2004 map is shown together with the proper motion velocities. N is up and E to the left.

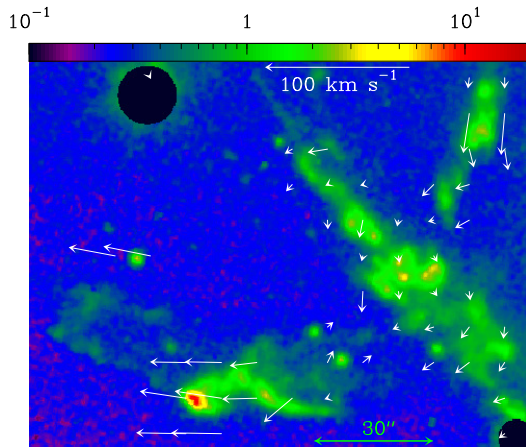


Figure 8. Subfield D of Figure 4. The 2004 map is shown together with the proper motion velocities. N is up and E to the left.

in Figure 10), which might be associated with outflow 9 (see Figure 4).

4.7. Proper motions for the outflows of Davis et al. (2008)

As described above, we detect proper motions for knots which are likely to be associated with several of the outflows of Davis et al. (2008). These outflows are numbered 1 through 9 in Figure 4.

For each of these outflows, the following results are obtained:

- *outflow 1* - we measure proper motions of up to 20 km s^{-1} along the SE lobe of this outflow. These proper motions are consistent with the optical proper motions measured for HH 7-11 by Noriega-

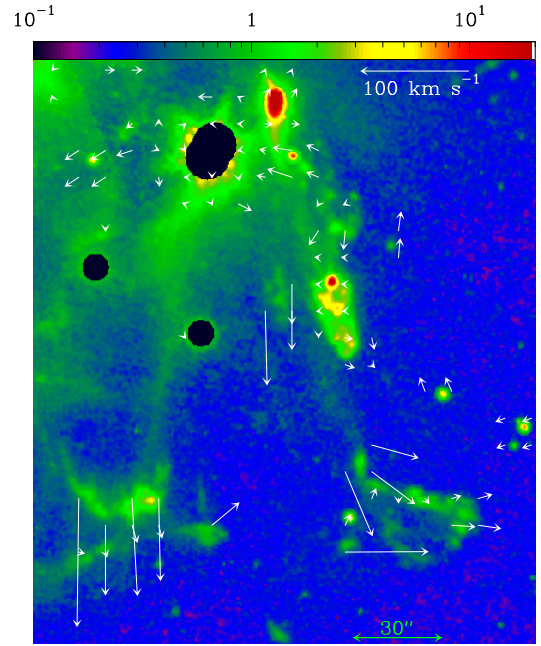


Figure 9. Subfield E of Figure 4. The 2004 map is shown together with the proper motion velocities. N is up and E to the left.

Crespo & Garnavich (2001). We do not see organized motions in the region that would correspond to the NW lobe of this outflow,

- *outflow 2* - we detect two sets of knots (within regions B and C of Figure 4, respectively) with proper motions of up to $\sim 100 \text{ km s}^{-1}$ aligned with the SE lobe of this outflow,
- *outflow 3* - we detect proper motions along both the E (region D) and W (region E) lobes of this outflow, with velocities of up to $\sim 80 \text{ km s}^{-1}$,
- *outflow 4* - we detect a Southern bow shock with proper motions of $\sim 100 \text{ km s}^{-1}$ (region E) and possibly a Northern bow shock with much lower ($\sim 10 \text{ km s}^{-1}$) velocities (region A), which might be associated with this outflow,
- *outflow 5* - we detect knots with velocities of $\sim 30 \text{ km s}^{-1}$ which might be associated with the Southern lobe of this flow (region D),
- *outflow 6* - we detect knots with proper motions of $\sim 50 \text{ km s}^{-1}$ which are likely to be associated with the Northern (region A) and Southern (region E) lobes of this outflow,
- *outflow 7* - the E lobe of this outflow coincides with IR knots with velocities of $\sim 15 \text{ km s}^{-1}$,
- *outflow 8* - we do not obtain proper motion velocities aligned with this outflow,
- *outflow 9* - we marginally detect proper motion velocities of $\sim 10 \text{ km s}^{-1}$ which might be associated with this outflow.

Therefore, we detect knots with measurable proper motions which are likely to be associated with all but one of the outflows of Davis et al. (2008).

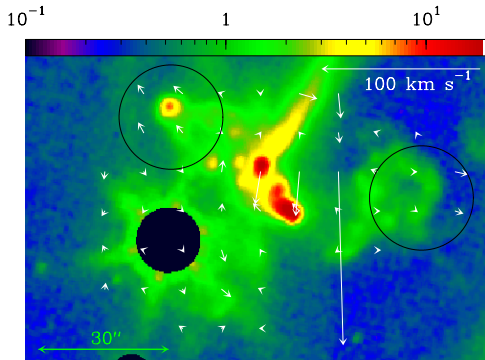


Figure 10. Subfield F of Figure 4. The 2004 map is shown together with the proper motion velocities. The two open circles indicate the regions that could be associated with the two lobes of outflow 9 (see section 4.6). N is up and E to the left.

4.8. The proper motion velocity distribution function

If we are detecting most of the outflows in NGC 1333, the measured proper motion velocities v_T allow us to obtain the distribution function associated with the outflows from a group of stars currently being formed. If we consider the maximum value of v_T for the 8 outflows of Davis et al. (2008) with measured proper motions (see subsection 4.7), we find that we have 3 with maximum v_T in the $0 \rightarrow 20 \text{ km s}^{-1}$ range, 1 outflow in each of the $20 \rightarrow 40$, $40 \rightarrow 60$ and $60 \rightarrow 80 \text{ km s}^{-1}$ ranges, and 2 outflows with v_T in the $80 \rightarrow 100 \text{ km s}^{-1}$ range. The resulting distribution function (normalized to a total of 5 outflows, see below) is shown in Figure 11.

The distribution function shows an apparent peak at low proper motion velocities (v_T), and possibly also a marginal peak in the higher velocity bin. One can show that this distribution is not consistent with a set of outflows with identical intrinsic velocities v_j and with arbitrary orientation angles with respect to the plane of the sky.

It is straightforward to show that if we have a set of outflows with outflow velocity v_j and with arbitrary orientations, the expected distribution function for the proper motion velocities v_T is:

$$f(v_T) = \frac{1}{v_j} \left[\left(\frac{v_j}{v_T} \right)^2 - 1 \right]^{-1/2} \quad (1)$$

This distribution function is plotted in Figure 11, considering $v_j = 100 \text{ km s}^{-1}$. In this Figure, the distribution function obtained from the 8 observed outflows has been normalized to 5 outflows, i.e., not considering the 3 outflows in the $0 \rightarrow 20 \text{ km s}^{-1}$ bin. A comparison between the observed and theoretical distributions shows that a single population of $v_j = 100 \text{ km s}^{-1}$ outflows (at random orientations) does not produce a proper motion velocity distribution consistent with the data.

Particularly, from Figure 11 it is clear that the observed outflows have a large population in the lowest velocity bin ($0 \rightarrow 20 \text{ km s}^{-1}$), for which the “ $v_j = 100 \text{ km s}^{-1}$ model” predicts low frequencies. This large population of the lowest proper motion velocity bin therefore implies that some of the outflows in our group indeed have a low, full spatial velocity, of at most $v_j \sim 20 \text{ km s}^{-1}$.

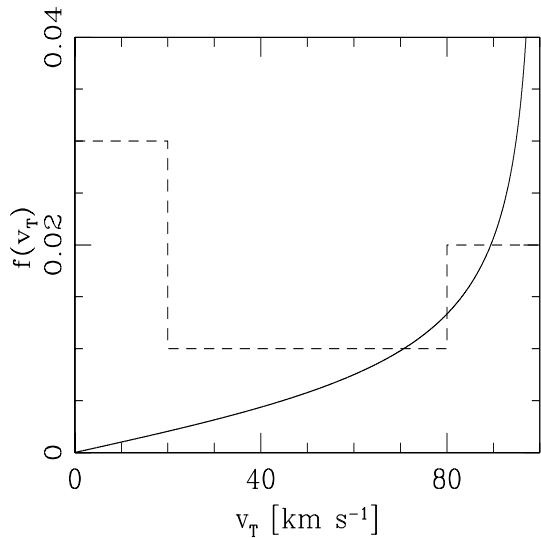


Figure 11. The dashed histogram shows the distribution function obtained by binning the peak proper motion velocities of the 8 outflows of Davis et al. (2008) which we have detected, normalized to a total of only 5 outflows. The solid curve is the distribution function expected for a set of outflows of intrinsic velocity $v_j = 100 \text{ km s}^{-1}$ at random orientations (see equation 1).

5. SUMMARY AND CONCLUSIONS

In this paper, we present a first attempt to derive proper motions of young stellar outflows from Spitzer (IRAC) images. Our analysis of the NGC 1333 region (which includes the HH 7-11 outflow) shows that it is indeed possible to do this, which opens up the possibility of obtaining new “second epoch” observations with Spitzer, in order to derive proper motions for a relatively larger number of IR outflows.

We have analyzed two epochs at a time interval of ≈ 7 yr, and the fact that proper motions are indeed detected can be seen by taking the difference between the two frames (see Figure 1). Using these two frames, we first derive the proper motions of HH 7, 8 and 10.

The resulting proper motions correspond to plane of the sky velocities of $\approx (10 \pm 4) \text{ km s}^{-1}$ (see Figure 3 and section 3), at a distance of 220 pc, which are consistent with the optical proper motions of these objects derived by Herbig & Jones (1983) and Noriega-Crespo & Garnavich (2001). Our results do not agree with the $\sim 400 \text{ km s}^{-1}$ IR proper motions of Chrysostomou et al. (2000).

We have then derived proper motion velocities for the emission knots in a $450 \times 550''$ field, many of which are aligned with the outflows described by Davis et al. (2008). For one of these outflows (outflow 3, see Figure 4), we find a clear bipolar motion (with velocities of $\sim 80 \text{ km s}^{-1}$). The CO emission of this outflow is clearly seen in the observations of Curtis et al. (2010). Another remarkable result is the $\sim 100 \text{ km s}^{-1}$ velocity derived for the Southern bow shock of outflow 3 (see Figures 4 and 9).

From the proper motions of the 8 outflows of Davis et al. (2008) for which we have measurements, we obtain a proper motion velocity distribution function (see section 4.8). We find that this distribution function is not consistent with a set of outflows with identical outflow velocities (of $\sim 100 \text{ km s}^{-1}$) at random orientations. The

empirically derived distribution function indicates that some of the observed outflows have intrinsic outflow velocities $v_j \sim 100 \text{ km s}^{-1}$, and that others have a much lower, $v_j \sim 10\text{-}20 \text{ km s}^{-1}$ velocity. This consists of a first suggestion that the velocities v_j (of a group of outflows from recently formed stars in the same cloud) have a bimodal distribution.

Even though the derived proper motions only give partial constraints on the kinematics of the outflows in NGC 1333, they do provide some of the information necessary for modelling this system. This is of particular interest, since it appears to be a case in which the outflows have a strong influence on the structure of their parental cloud, and might even be triggering the formation of more stars (see Sandell & Knee 2001). Some other clouds might also be in a regime of strong perturbation from the outflows from YSOs (see, e.g., Are et al. 2010; Duarte-Cabral et al. 2012).

It would be interesting to use the kinematics derived from our proper motion determinations to compute simulations of jet-driven turbulence such as the ones of Nakamura & Li (2007) and Carroll et al. (2010). Would we then obtain a perturbed cloud such as NGC 1333 (Sandell & Knee 2001; Arce et al. 2010)? This would be an interesting complement to the quite extensive work that has been done on this object (see the papers quoted above and Quillen et al 2005; Maret et al. 2009; Padoan et al. 2009; Arce et al. 2010).

This research is based in part on observations made with the *Spitzer Space Telescope* (NASA contract 1407) and has made use of the NASA/IPAC Infrared Science Archive, both are operated by the Jet Propulsion Laboratory, California Institute of Technology, under contract with the National Aeronautics and Space Administration (NASA). AR acknowledges support from the CONACyT grants 60526, 61547, 101356 and 101975. We thank Luisa Rebull & John Stauffer for useful conversations about their program. We also thank an anonymous referee for many corrections of the first version of this paper.

APPENDIX

Appendix A: Proper motion mapping

In order to derive proper motions from pairs of CCD images it has now become standard to define boxes including emitting “knots”, and to carry out cross-correlations (between the 2 frames) of the emission within the boxes. The proper motion is then obtained from a fit to the peak of the cross-correlation function. This method has proven to be better than carrying out direct fits (of e.g., a Gaussian or a 2D paraboloid) to the observed emission features, because the cross-correlation functions (which are integrals of the emission within the chosen boxes) have higher signal-to-noise ratios than the images.

For images with many knots, it is simpler to use a regular array of boxes (or “tiles”, as called by Szyszka et al. 2011) for computing cross correlations. Proper motions for the emission within each of the boxes are then obtained from fits to their respective cross-correlation functions.

In this paper, we use the setup described by Raga et al. (2012). We define square boxes of side L , with spacings of $L/2$ along each of the coordinates of the images. Therefore, neighbouring boxes have a superposition region of size $L/2$ along each axis, as shown in the schematic diagram of Figure 12.

For a given box of size L (see Figure 12), we first check whether or not the condition $f \geq f_{min}$ (where f is the intensity of the image and f_{min} is a user specified “minimum flux”) is satisfied in at least one pixel within a central “inner box” of size $L/2$. If this condition is met at least for a single pixel in each of the two epochs that are being analyzed, the cross-correlation function (within the L -size box in the two frames) and the proper motion (from a paraboloidal fit to 3×3 pixels centered on the peak of the cross correlation function) are computed.

Therefore, in order to compute a “cross correlation map”, it is then only necessary to specify the box size “ L ” and

REFERENCES

- Arce, H. G., Borkin, M. A., Goodman, A. A., Pineda, J. E. & Halle, M. W. 2010, ApJ, 715, 1170
 Carrol, J. J., Frank, A. & Blackman, E. G. 2010, ApJ, 722, 145
 Černis, K. 1990, A&SS, 166, 315
 Curtis, E. I., Richer, J. S., Swift, J. J. & Williams, J. P. 2010, MNRAS, 408, 1516
 Chrysostomou, A., Hobson, J., Davis, C. J., Smith, M. D. & Berndsen, A. 2000, MNRAS, 314, 229
 Davis, C. J., Scholz, P., Lucas, P., Smith, M. D. & Adamson, A. 2008, MNRAS, 387, 954
 Duarte-Cabral, A., Chrysostomou, A., Peretto, N., Fuller, G. A., Matthews, B., Schieven, G. & Davis, G. R. 2012, A&A, 543, 140
 Evans, N. J. II et al. 2009, ApJS, 181, 321
 Fazio, G. et al. 2004, ApJS, 154, 10
 Herbig, G. H. & Jones, B. F. 1981, AJ, 86, 1232
 Herbig, G. H. & Jones, B. F. 1983, AJ, 88, 1040
 Hirota, T. et al. 2008, PASJ, 60, 37
 Knee, L. B. G. & Sandell, G. 2000, A&A, 361, 671
 Looney, L. W., Tobin, J. J. & Kwon, W. 2007, ApJ, 670, 131
 Makovoz, D., Khan, I. & Masci, F. 2006, SPIE, 6065, 330
 Maret, S. et al. 2009, ApJ, 698, 1244
 Nakamura, F. & Li, Z.-Y. 2007, ApJ, 662, 395
 Noriega-Crespo, A. & Raga, A. C. 2012, ApJ, 750, 101
 Noriega-Crespo, A. et al. 2004, ApJS, 154, 352
 Noriega-Crespo, A. et al. 2004, ApJS, 154, 402
 Noriega-Crespo, A. & Garnavich, P. M. 2001, AJ, 122, 3317
 Noriega-Crespo, A., Garnavich, P. M., Curiel, S., Raga, A. C. & Ayala, S. 1997, ApJ, 486, L55
 Padoan, P., Juvela, M., Kritsuk, A., Norman, M. L. 2009, ApJ, 707, L153
 Quillen, A. C., Thorndike, S. L., Cunningham, A., Frank, A., Gutermuth, R. A., Blackman, E. G., Pipher, J. L., Ridge, N. 2005, ApJ, 632, 941
 Raga, A. C., Noriega-Crespo, A., Rodríguez-González, A., Lora, V., Stapelfeldt, K. R. & Carey, S. J. 2012, ApJ, 748, 103
 Raga, A. C., Noriega-Crespo, A., Lora, V., Stapelfeldt, K. R. & Carey, S. 2011 ApJ, 730, 17
 Raga, A. C., Barnes, P. J. & Mateo, M. 1990, AJ, 99, 1912
 Rodríguez, L. F., Curiel, S., Moran, J. M., Mirabel, I. F., Roth, M. & Garay, G. 1989, ApJ, 346, L85
 Sandell, G. & Knee, L. B. G. 2001, ApJ, 546, L49
 Szyszka, C., Zijlstra, A. A. & Walsh, J. R. 2011, MNRAS, 416, 715
 Tobin, J. J., Looney, L. W., Mundy, L. G., Kwon, W. & Hamidouche, M. 2007, ApJ, 659, 1404
 Ybarra, J. E. & Lada, E. A. 2009, ApJ, 695, 120
 Werner, M. W. et al. 2004, ApJS, 154, 1

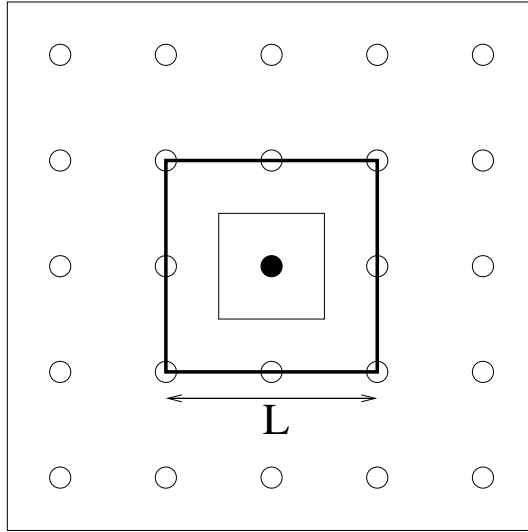


Figure 12. Schematic diagram showing one of the cross correlation boxes (thick line box, of size L). The solid circle is the central position of this box, and the open circles are the central positions of the nearby cross correlation boxes. The inner box (drawn with a thin line) of size $L/2$ is used for evaluating whether or not the peak flux satisfies the criterion for calculating a proper motion

Table 1
NGC 1333 Observations

Program ID	Request Key	Observation Time	PI
6	3652864	2004-02-10	Fazio, G.
178	5793280	2004-09-08	Evans, N.
61026 ^a	29323008	2011-10-12	Stauffer, J.
	29319424	2011-11-13	

^a There are 73 independent observations (Request Key) in this program; the first and last are shown.

the minimum flux f_{min} . Actually, there is another “hidden” parameter which is the centering of the quadratic of boxes with respect to the pixels of the image. This is fixed arbitrarily so that the first pixel of the frames that are being studied coincides with the edge of one of the cross-correlation boxes.

We find that the peaks of the cross correlation boxes can be fitted to within ~ 0.1 pixel, a precision similar to the one of the alignment between the two epochs that we have used. Therefore, the formal errors of our proper motion determinations are of ~ 0.1 pixel, corresponding to a velocity of $\sim 4 \text{ km s}^{-1}$.